Optical bistability in a multiple-quantum-well structure with Fabry-Pérot and distributed-feedback resonators

G. P. Bava
Dipartimento di Elettronica, Politecnico di Torino, Corso Duca degli Abruzzi 24, 10129, Torino, Italy

F. Castelli*
Dipartimento di Fisica, Politecnico di Torino, Corso Duca degli Abruzzi 24, 10129, Torino, Italy

P. Debernardi
Centro Studi Propagazione Antenne, Consiglio Nazionale delle Ricerche, c/o Politecnico di Torino, Corso Duca degli Abruzzi 24, 10129 Torino, Italy

L. A. Lugiato*
Max-Planck Institut für Quantenoptik, D-8046 Garching, Germany
(Received 12 August 1991)

The system we analyze has the structure of a planar optical waveguide containing a multiple quantum well, with the planes of the wells parallel to the direction of propagation. We consider the two different configurations of a Fabry-Pérot cavity and distributed-feedback device. The optical nonlinearities are described by means of the first-principles theory developed by Haug, Koch, Schmitt-Rink, and coworkers, generalized to include the finite width of the wells. The dynamics of the system is described by the equations that govern the evolution of the two counterpropagating fields, coupled with the carrier-density equation, and accompanied by the appropriate boundary conditions. The steady-state behavior is analyzed as a function of the control parameters of the system for the case of a $GaAs/Al_{1-x}Ga_xAs/AlAs$ structure. The system develops bistability even when the input field is in resonance with the excitonic peak, but the phenomenon becomes more pronounced in the detuned configuration. The hysteresis cycles obtained in the case of distributed-feedback device turn out to be competitive with those displayed by the Fabry-Pérot system.

PACS number(s): 42.65.Pc, 78.65.−s, 42.79.Ta

I. INTRODUCTION

The phenomenon of optical bistability (OB) and its relevance to the fields of optical information processing and optical computing are by now well known [1–3]. The most classic configuration for this phenomenon is that of a nonlinear medium placed in a resonant Fabry-Pérot cavity and driven by a stationary coherent field injected into the cavity.

It is customary to distinguish two extreme cases that are usually designated with the names of *absorptive bistability* and *dispersive* (or *refractive) bistability,* respectively. In the absorptive case the input field is exactly resonant with the absorption line of the medium and refractive effects are absent; the bistable behavior arises from the intensity dependence of the absorption coefficient, which produces the saturation of the material. On the other hand, in the dispersive case the medium is transparent (i.e., no absorption), and bistability arises from the intensity dependence of the refractive index, which produces the shift of a cavity frequency toward resonance with the input field. Dispersive OB is preferable because it is more easily controllable, for it does not require saturation (a nonlinear refractive index of the Kerr-medium type; i.e., $n=n_0+n_2I$ is enough), and because of the absence of heating problems. Unfortunately, the presence of some level of absorption is unavoidable and this circumstance limits and degrades the performance of the system. Paradigmatic is the two-level model of OB [2,4] which includes both absorptive and dispersive effects; it shows that absorptive OB produces larger hysteresis cycles for the transmitted power as a function of the incident power, but dispersive OB requires smaller values of the input power to make the system switch from the lower to the upper branch of the cycle.

In recent years a great interest has emerged about optical nonlinear effects in semiconductor materials, in particular in structures including multiple quantum wells (MQW) [3,5–7]. Among the most important characteristics of such materials one can mention the very strong nonlinearity when the operating frequency is near an excitonic resonance, that is, the resonance of the electromagnetic field with an electron-hole bound state due to the Coulomb interaction; the corresponding frequency appears just below the band gap (on the order of 10 meV). This strong nonlinearity, in MQW structures, also persists at room temperature, while in bulk materials it can be observed only at a very low temperature [5,7,8]. This property makes MQW structures very attractive for the application to nonlinear photonic and/or electro-optic devices.

Experimental evidence of bistable behavior in FP resonators, in which a MQW is inserted, was reported several years ago [3] and was the subject of several papers, for instance, [3,7,9,10–12]; recent very interesting experimental results in a reflection configuration are given in [13]. Much work on bistable effects in distributed-feedback structures has been recently reported [14–18].

The presence of the excitonic resonance makes MQW systems somewhat similar to the case of two-level atoms; as a matter of fact, the dynamical equations for OB in MQW systems become equivalent to the two-level model, when the excitonic contribution to the dielectric constant is factorized into a term which depends on the frequency and a term which depends on the carrier density N, and the N-dependent factor is assumed linear [19]. The smallness of the saturation intensity for the excitonic peak suggests the feasibility of absorptive OB for this system; however, the continuum band-to-band transitions also contribute to the dielectric constant and enhance the absorption of the material. Also dispersive bistability is feasible by detuning the input frequency to the low-frequency side of the excitonic peak; the residual absorption, however, may degrade the bistable behavior or even destroy it.

The investigation of this problem has been carried out using simplified models which assume a cubic nonlinearity [12] or a saturable nonlinearity [10]. In order to identify the optimal conditions to achieve bistability in MQW structures we prefer to base our analysis on a model which ensures an adequate description of the optical nonlinearity in these systems. This sophisticated model, which has been elaborated by Haug, Koch, Schmitt-Rink, and co-workers [20–25], starts from a first-principles microscopic description and allows for the evaluation of the contribution $\Delta\epsilon$ to the dielectric constant, which arises from both excitonic and band-to-band transitions, as a function of frequency, of the carrier density and of the parameters of the material. In this paper we use an extension of this model, which includes the effect of finite well thickness.

The system we analyze has the structure of a planar optical waveguide containing a MQW in the core region [Fig. 1(a)], with the planes of the wells parallel to the direction of propagation. We consider the two different configurations of Fabry-Pérot cavity [FP, Fig. 1(b)] and distributed feedback device [DFB, Fig. 1(c)]. In the FP case the feedback is provided by the mirrors at the endfacets of the sample; in the DFB case the feedback is produced by the grating built in the structure in the longitudinal direction. In both cases we study the behavior of the transmitted power as a function of the input power at steady state; due to the strong nonlinear absorption and refraction effects near the excitonic resonance, the adopted model accounts for the wave propagation inside the resonator.

Examples of numerical computations will be reported by varying some significant parameters of the devices, such as mirror reflectivity, grating features, cavity length, and detuning of the optical signal with respect to the unperturbed cavity resonance. For uniformity all the results will refer to a $GaAs/Al_{1-x}Ga_xAs/AlAs$ structure. For the sake of simplicity we do not consider the grating in the carrier density produced by the standing wave structure of the field, assuming that the grating is washed out by diffusion. In the evaluation of the optical response we consider a simplified band structure including only one conduction and one valence subband, and accordingly we account for the electron–heavy-hole exciton only.

In Sec. II we review the model for optical nonlinearities in MQW structures, formulated by Haug, Koch, Schmitt-Rink, and co-workers, and its generalization to the case of wells with a finite width [26]. The absorption coefficient and the refractive index are calculated as a function of frequency and carrier density. Section III discusses the coupled dynamical equations for the counterpropagating field and for the carrier density, the appropriate boundary conditions for the fields in the FP and DFB cases, and the techniques to solve numerically the equations at steady state. The numerical results are described in Sec. IV, while Sec. V illustrates and discusses the main conclusions of our work.

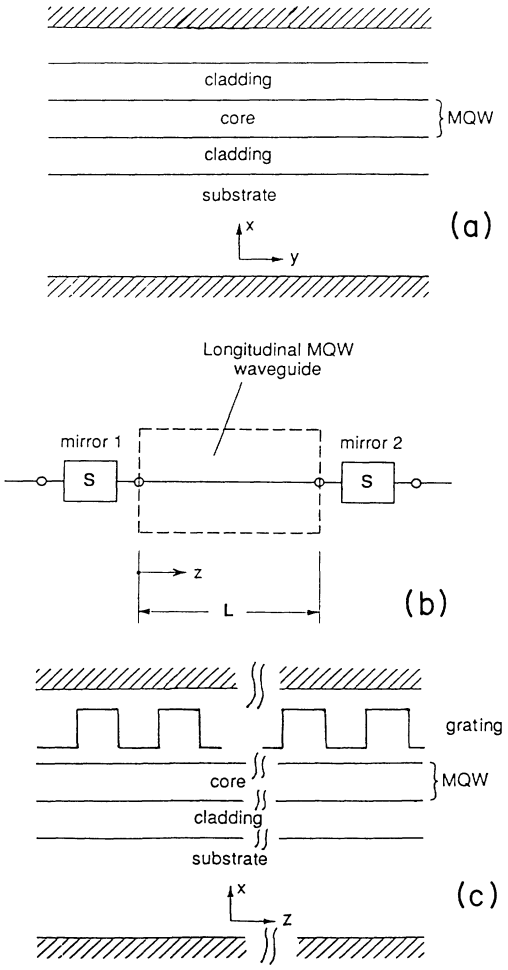

FIG. 1. (a) Schematic waveguide cross section; (b) longitudinal representation of the FP resonator; (c) longitudinal representation of the DFB device.

II. QW OPTICAL RESPONSE

The nonlinear dielectric response in MQW structures is due to a combination of many-body effects such as the Coulomb interaction between carriers and the exclusion principle [5,8,20,22,23]; the most important aspects of the many-body behavior, at room temperature, are represented by the renormalization of the band gap and the screening of the Coulomb interaction at increasing carrier density. As a consequence the optical nonlinearity is directly related to the carrier density generated by the optical absorption.

In the present paper the optical nonlinearity is evaluated by means of a model which accounts for only one conduction and one valence subbands, but includes correctly the effects of the finite well thickness [26]. Under the preceding conditions the contribution $\Delta\epsilon$ to the dielectric constant ϵ, due to the interaction of the electromagnetic field at the angular frequency ω with the carrier density per unit area N in a well of thickness d, is given by

$$\Delta\epsilon(\omega,N)=\frac{2}{V}\sum_{\mathbf{k}}\mu_k\chi_k \tag{1}$$

with V being the volume under analysis ($=Ad$, with A reference area), $\mathbf{k}$ the particle wave vector parallel to the QW layer, μ_k the dipole matrix element between conduction and valence band at a given wave vector k [27] and for TE polarization. The microscopic polarization χ_k satisfies the equation [24]

$$\chi_k=\chi_k^0\left[1+\frac{1}{\mu_k}\sum_{\mathbf{k}'}V_{s,e\text{-}h}(|\mathbf{k}-\mathbf{k}'|)\chi_{\mathbf{k}'}\right], \tag{2}$$

where χ_k^0 is the corresponding quantity without Coulomb interaction which, adopting a spectral representation [24], can be written as

$$\chi_k^0(\omega)\simeq-\mu_k\frac{[1-f_e(E_e)-f_h(E_h)](\hbar\omega-E_{cv})-i\gamma_k[1-f_e(\hbar\omega-E_g-E_h)-f_h(E_h)]}{(\hbar\omega-E_{cv})^2+\gamma_k^2}.$$

In the preceding equation f_e and f_h are, respectively, the Fermi distributions of electrons (e) and holes (h), with $E_e(k)$ and $E_h(k)$ being the corresponding energies and E_g the unperturbed bidimensional band gap. The quantity $E_{cv}(k)=E_e(k)+E_h(k)+E_g'$ denotes the energy difference between the conduction- and the valence-band states at the same k and included the band-gap renormalization ΔE_g ($E_g'=E_g+\Delta E_g$) [23]; γ_k is a dynamical damping approximated by the following expression [24,28]:

$$\gamma_k(\omega)=\frac{2\gamma_0}{1+e^{(E_{cv}-\hbar\omega)/k_BT}}$$

with γ_0 properly chosen. Finally $V_{s,e\text{-}h}(q)=V_{e\text{-}h}(q)/\epsilon_s(q,\omega)$ is the screened Coulomb potential; for ϵ_s a static, single-plasmon pole approximation was adopted [23]. $V_{e\text{-}h}(q)$ is the Fourier transformed Coulomb potential, which takes the form [29]

$$V_{e\text{-}h}(q)=V_{2D}(q)\int_{z_e}\int_{z_h}\epsilon_w\epsilon^{-1}(z_e,z_h)|\Phi_e(z_e)|^2|\Phi_h(z_h)|^2\times e^{-q|z_e-z_h|}dz_e dz_h . \tag{3}$$

In the preceding equation Φ_e and Φ_h are the electron and hole normalized wave functions in the potential well. In the limit case when the well thickness $d\to 0$ and the potential well height $\to\infty$ the preceding expression reduces to the more familiar 2D potential $V_{2D}(q)=e^2/2qA\epsilon_w$. In the above expression multiple image effects have been neglected and the static dielectric constant $\epsilon(z_e,z_h)$ has been approximated by its well value ϵ_w when both coordinates z_e and z_h lie inside the well, by the barrier value when both coordinates z_e and z_h lie out of the well, and by an appropriately weighted value in the other cases. The band-gap renormalization owing to the electron-hole plasma is computed as [23]

$$\Delta E_g=\sum_q\left[\tfrac{1}{2}(V_{s,e\text{-}e}-V_{e\text{-}e})+\tfrac{1}{2}(V_{s,h\text{-}h}-V_{h\text{-}h})-(V_{s,e\text{-}e}f_{eq}+V_{s,h\text{-}h}f_{hq})\right],$$

where the quantities $V_{s,e\text{-}e}$ and $V_{s,h\text{-}h}$ are analogous to $V_{s,e\text{-}h}$ and, in the same way, $V_{e\text{-}e}$ and $V_{h\text{-}h}$ are analogous to $V_{e\text{-}h}$; for example, $V_{e\text{-}e}$ is defined as Eq. (3) by replacing Φ_h by Φ_e and z_h by z_e'; note that in our model ΔE_g is d dependent through the Coulomb potential.

The choice of the well thickness plays a very important role; on one hand too small values of d give rise to a vanishing contribution of the MQW effect both due to the spreading of the wave functions in the barriers and to the decreasing value of the overlap integral with the electric field of the guided mode; on the other hand, by increasing d the effect of the well becomes less and less effective as regards the excitonic interaction. As a consequence an optimum value of d can be expected; for GaAs-based structures and with respect to the absorption and refractive index variation, such an optimum corresponds approximately to $d\simeq 50$ Å [26].

Equation (2) is solved by approximating the sum with an integral and by solving the resulting integral equation. The numerical technique expands the unknown function in terms of Chebichev polynomials and solves the corresponding set of linear algebraic equations for the expansion coefficients. For a GaAs/$Al_{1-x}Ga_xAs$ QW struc-

ture, using the numerical values for the material parameters given in Ref. [24], the absorption [related to $\mathrm{Im}(\Delta\epsilon)$] and the refractive index [related to $\mathrm{Re}(\Delta\epsilon)$] spectra are shown, respectively, in Figs. 2(a) and 2(b), for several values of carrier density N (multiplied by the square of the 2D exciton Bohr radius a_0). The abscissa Δ is defined as

$$\Delta=\frac{\hbar\omega-E_{g2D}}{E_x} ,$$

where E_{g2D} is the 2D band gap and E_x the 2D exciton binding energy. In particular, in Fig. 2(a), the exciton resonance peak and its bleaching at increasing carrier density are well evident.

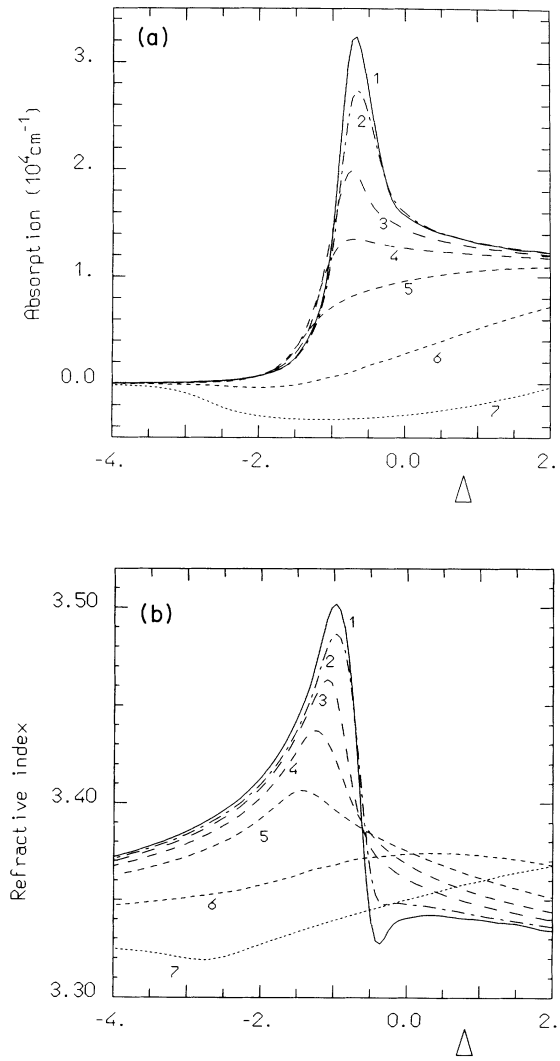

FIG. 2. Absorption (a) and refractive index (b) spectra for a $GaAs/Al_{1-x}Ga_xAs$ QW for several values of carrier density (multiplied by the square of the two-dimensional exciton Bohr radius a_0); (1) $Na_0^2=0$, (2) $Na_0^2=0.01$, (3) $Na_0^2=0.05$, (4) $Na_0^2=0.1$, (5) $Na_0^2=0.2$, (6) $Na_0^2=0.5$, (7) $Na_0^2=1.0$.

III. MODEL FOR THE NONLINEAR INTERACTION

A. Model equations

The nonlinearity in the field-carrier interaction and the effect of a possible grating, in the DFB case, will be introduced perturbatively through coupled-mode theory [30], but considering only a single transverse mode (in our case the TE_0) of the optical waveguide whose cross section is shown in Fig. 1(a). In practical situations, this assumption is rather satisfactory since the coupling to other modes is very small and, moreover, we can suppose that the waveguide has been designed to work in monomodal conditions. In the framework of the coupled-mode approach, if $C_F(z,t)$ and $C_B(z,t)$ denote the slowly varying (in the z direction and in time) amplitudes of the forward and backward traveling waves, respectively (normalized so that their squared moduli correspond to the traveling power per unit guide width), the following equations hold [3,14,30] (for a sketch of derivation see the Appendix):

$$\frac{\partial C_F}{\partial z}+\frac{1}{v_g}\frac{\partial C_F}{\partial t}=+[h(z)-\alpha_i]C_F+KC_Be^{-i\Delta\beta z} , \quad (4a)$$

$$\frac{\partial C_B}{\partial z}-\frac{1}{v_g}\frac{\partial C_B}{\partial t}=-[h(z)-\alpha_i]C_B+K^*C_Fe^{i\Delta\beta z} , \quad (4b)$$

where v_g is the mode group velocity, α_i is the mode attenuation due to the material intrinsic losses (excluding the interaction with the carriers); the self-coupling coefficient $h(z)$, which accounts for the optical field coupling to the electrons and holes represented by $\Delta\epsilon$ [see Eq. (1)], is given by

$$h=\frac{i\omega m}{2v_g}\frac{\int_d\Delta\epsilon|E_0|^2dx}{\int\epsilon|E_0|^2dx} , \quad (5)$$

where m represents the number of wells of thickness d and E_0 describes the mode field distribution. Note that the function $h(z)$ includes a spatial averaging over the region inside and outside the wells.

The coupling coefficient K between forward and backward waves due to a possible grating, characterized by a dielectric constant variation $\Delta\epsilon_g$ with respect to the reference waveguide (see the Appendix), is obtained as

$$K=\frac{i\omega}{2v_g}\frac{\int_g\Delta\epsilon_g^{(p)}|E_0|^2dx}{\int\epsilon|E_0|^2dx} , \quad (6)$$

where $\Delta\epsilon_g^{(p)}$ is the spatial harmonic which satisfies in the best way the Bragg condition $2\beta_0\simeq 2\pi p/\Lambda=p\beta_g$ with β_0 being the mode propagation constant, Λ and β_g being, respectively, the period of the grating and the corresponding propagation constant; p is an integer number which defines the spatial harmonic of interest. In the denominators of Eqs. (5) and (6) the integral represents the stored electric energy in the modal field distribution; in the numerators the integrals are extended to the x range where $\Delta\epsilon$ and $\Delta\epsilon_g^{(p)}$ are different from zero (that is, respectively, one well and the grating region, if any; we as-

sume, for simplicity, that all the wells are equivalent from the point of view of the interaction). The quantity $\Delta\beta=2\beta_0-p\beta_g$ denotes the detuning between the operating propagation constant and the one corresponding to the Bragg condition.

In the case of a conventional FP resonator $K=0$; so Eqs. (4) hold for both the FP and DFB structures, but clearly they must be associated with different boundary conditions (see following subsections). Equations (4) must be coupled to the evolution equation for $N(z,t)$, on which $\Delta\epsilon$ and, consequently, h depend. So we introduce the rate equation for the carriers in a well [19]:

$$\frac{\partial N}{\partial t}=-R(N)+\mathrm{Im}\left[\frac{\Delta\epsilon(N)}{\epsilon}\right](\hbar v_g)^{-1}\eta(|C_F|^2+|C_B|^2)\ , \tag{7}$$

where $R(N)=AN+BN^2$ accounts for the recombinations. The confinement factor η reads

$$\eta=\frac{\int_d \epsilon|E_0|^2dx}{\int \epsilon|E_0|^2dx} \tag{8}$$

and it is the measure of the amount of electrical power in a well with respect to the total mode power. The second term on the right-hand side of Eq. (7) accounts for optical carrier generation; more rigorously the carrier diffusion effects along z should be included and also the spatial grating due to the beat of forward and backward waves; for simplicity it has been assumed that diffusion compensates such a grating, since the diffusion length is larger than the grating period.

Equations (4) and (7) have been written including the dynamical aspects; however, in the remainder of this paper only static solutions will be discussed and therefore the derivatives with respect to time will be dropped.

The material characteristics depend on ω and N through Eq. (1); by means of Eq. (7), without time derivative, the carrier density can be related to the "local optical power" $P_l=|C_F|^2+|C_B|^2$. So it can be of interest to analyze the dependence of the carrier density N, the absorption coefficient α, and the refractive index difference Δn as a function of P_l. The waveguide parameters that appear in our model are only the number of wells m and the confinement factor η. The numerical values adopted for those parameters are $m=6$ and $\eta=0.0177$ (which can be considered typical for a refractive index profile as in Fig. 15, with six wells of thickness $d=50$ Å). In addition, in the subsequent analysis and calculations, we use the following numerical values for the bulk material parameters: $A=0.2\times10^9\ \mathrm{s}^{-1}$ and $B=5\times10^{-4}\ \mathrm{cm}^2\mathrm{s}^{-1}$ for the recombination term of Eq. (7), and $\alpha_i=2.5\ \mathrm{cm}^{-1}$ for the intrinsic attenuation.

In Figs. 3, 4, and 5 the quantities α, Δn, and Na_0^2 are shown, respectively, as a function of P_l (in mW/μm) for $\Delta=-3$, -2, -1, and -0.7. The last choice corresponds to the exciton absorption peak [see Fig. 2(a)]. The inserts in Figs. 3 and 4 give the same diagrams but in an expanded logarithmic abscissa scale, to put in evidence some particular behavior for very low power levels.

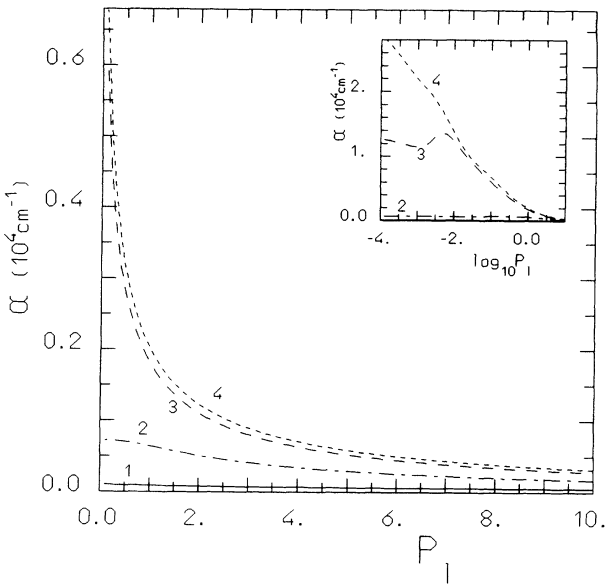

FIG. 3. Absorption coefficient α as a function of the local power P_l (in mW/μm) for (1) $\Delta=-3$, (2) $\Delta=-2$, (3) $\Delta=-1$, (4) $\Delta=-0.7$. The insert is the same diagram with logarithmic abscissa scale.

Clearly the absorption (Fig. 3) is very high near the excitonic peak and saturates at increasing P_l. At $\Delta=-1$ an inversion occurs, showing a small region of absorption increasing with power as a consequence of the band-gap renormalization.

A similar behavior can be observed as regards Δn in Fig. 4. However a still relevant change of Δn with P_l is achieved for Δ values well below the excitonic resonance,

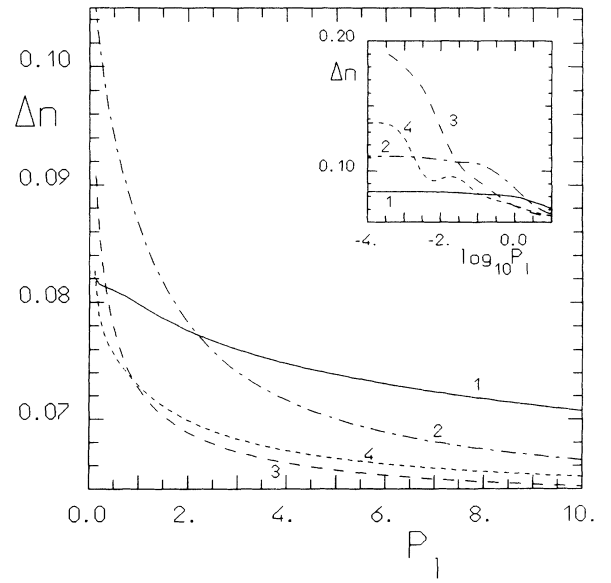

FIG. 4. Refractive index difference Δn as a function of the local power P_l (in mW/μm) for (1) $\Delta=-3$, (2) $\Delta=-2$, (3) $\Delta=-1$, (4) $\Delta=-0.7$. The insert is the same diagram with logarithmic abscissa scale.

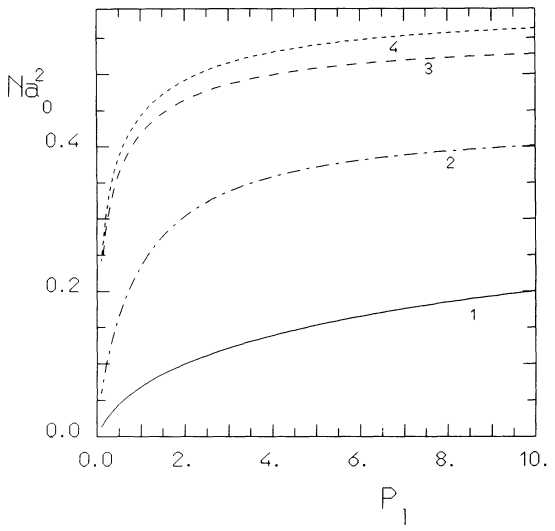

FIG. 5. Normalized density of carriers Na_0^2 as a function of the local power P_l (in mW/μm) for (1) $\Delta=-3$, (2) $\Delta=-2$, (3) $\Delta=-1$, (4) $\Delta=-0.7$.

where the absorption is very small. This fact allows to exploit the optical response of QW structures for refractive optical bistability.

B. FP case

The usual FP resonator corresponds to no distributed coupling between C_F and C_B, i.e., $K=0$ in Eq. (4), and the resonant characteristics are connected to the multiple reflections between the mirrors [Fig. 1(b)]. For the problem under consideration the boundary conditions can be expressed by the scattering parameters S_{ij} of the two mirrors, supposed symmetrical; $S_{11}=S_{22}$ are the mirror reflection coefficients at their two facets; $S_{12}=S_{21}$ are the mirror transmission coefficients. With the previous assumptions one can write [3]

$$\begin{aligned} C_F(0)&=S_{21}C_i+S_{11}C_B(0)\ , \\ C_B(L)&=e^{2i\beta_0 L}S_{11}C_F(L)\ , \\ C_r&=S_{11}C_i+S_{21}C_B(0)\ , \\ C_t&=S_{21}C_F(L)\ , \end{aligned} \tag{9}$$

where C_i, C_r, and C_t are, respectively, the incident, reflected, and transmitted amplitudes outside the resonator, and β_0 is the propagation constant of the input field, which has angular frequency ω.

For the problem under examination, in the stationary case, a partially analytical solution can be carried out, which can substantially reduce the computer time for a complete evaluation of the device performance. In fact, with $K=0$ and $\partial/\partial t=0$, Eqs. (4) can be formally integrated as follows:

$$\begin{aligned} C_F(z)&=C_F(0)\exp\left[-\alpha_i z+\int_0^z h(\xi)d\xi\right]\ , \\ C_B(z)&=C_B(0)\exp\left[+\alpha_i z-\int_0^z h(\xi)d\xi\right]\ , \end{aligned} \tag{10}$$

where, clearly, the complete solution requires the determination of the function $N(z)$ on which $h(z)$ depends. Taking into account Eqs. (10) and the boundary conditions (9), it is rather easy to obtain the following relations between the transmitted power $|C_t|^2$ and the incident ($|C_i|^2$) and reflected ($|C_r|^2$) powers, respectively:

$$|C_t|^2=|C_i|^2\frac{|S_{21}|^4\exp\left[-2\int_0^L(\alpha+\alpha_i)dz\right]}{\left|1-S_{11}^2\exp\left[-2L(-i\beta_0+\alpha_i)+2\int_0^L h(z)dz\right]\right|^2}\ , \tag{11}$$

$$|C_r|^2=|C_t|^2\frac{|S_{11}|^2}{|S_{21}|^4}\exp\left[2\int_0^L(\alpha+\alpha_i)dz\right]\left|1+(S_{21}^2-S_{11}^2)\exp\left[-2L(-i\beta_0+\alpha_i)+2\int_0^L h(z)dz\right]\right|^2\ , \tag{12}$$

where $\alpha=-\,\mathrm{Re}(h)$ and L is the resonator length [see Fig. 1(b)]. Because the longitudinal modes of the cavity with equal mirrors are defined by the condition

$$2\beta_c L+2\sigma_{11}=2\pi n,\quad n=0,1,2,\ldots,$$

where we have set

$$S_{11}=|S_{11}|e^{i\sigma_{11}},\quad S_{21}=|S_{21}|e^{i\sigma_{21}}$$

with

$$\sigma_{11}-\sigma_{21}=+\frac{\pi}{2}\text{or}-\frac{\pi}{2},\quad |S_{11}|^2+|S_{21}|^2=1\ ,$$

Eqs. (11) and (12) can be rephrased in the form

$$|C_t|^2=|C_i|^2\frac{|S_{21}|^4\exp\left[-2\int_0^L(\alpha+\alpha_i)dz\right]}{\left|1-|S_{11}|^2\exp\left[-i\delta-2\int_0^L[\alpha_i-h(z)]dz\right]\right|^2}\ , \tag{13}$$

$$|C_r|^2=|C_t|^2\frac{|S_{11}|^2}{|S_{21}|^4}\exp\left[2\int_0^L(\alpha+\alpha_i)dz\right]\left|1-\exp\left[-i\delta-2\int_0^L[\alpha_i-h(z)]dz\right]\right|^2, \tag{14}$$

where δ is the cavity detuning parameter

$$\delta=(\omega_c-\omega)2L/v_g \tag{15}$$

and $\omega_c=v_g\beta_c$ denotes the longitudinal cavity frequency (evaluated by using the bulk value for the refractive index, see Fig. 15) nearest to the input field frequency ω (hence by definition $|\delta|<\pi$). It appears immediately that the preceding Eqs. (13) and (14) are a generalization of the usual input-output relations for a FP resonator when h is not dependent on z.

Equations (13) and (14) allow a complete solution to the problem under consideration, provided that $N(z)$ [and hence $h(z)$] is known. The equation which determines $N(z)$ is obtained from the rate equation (7); after elimination of $|C_F|^2$ and $|C_B|^2$ by means of (9) and (10) one obtains

$$R(N)-\frac{\eta}{\hbar v_g}\frac{|C_t|^2}{|S_{21}|^2}\left[\exp\left[2\int_z^L(\alpha+\alpha_i)dz'\right]+|S_{11}|^2\exp\left[-2\int_z^L(\alpha+\alpha_i)dz'\right]\right]\mathrm{Im}\left[\frac{\Delta\epsilon(N)}{\epsilon}\right]=0, \tag{16}$$

which is a nonlinear integral equation for N, depending parametrically on $|C_t|^2$.

From this partially analytic formulation it appears that the strategy of solution of the nonlinear system is the following. First of all Eq. (16) is solved numerically in order to obtain $N(z)$ as a function of the transmitted power. An iterative technique has been used for the integral equation along z starting from a constant value of $N(z)$ till the convergence of the solution. As an example, in Fig. 6, the distribution of normalized carrier density Na_0^2 on the longitudinal coordinate z of the FP device is reported for several values of the output power. One sees clearly the strong optical absorption at low power levels and its saturation as the incident power is increased. Once $N(z)$ is known from the above procedure, one can compute $|C_i|^2$ and $|C_r|^2$ as a function of $|C_t|^2$ from Eqs. (13) and (14); by inverting the first function one obtains finally the transmission and reflection responses of the nonlinear resonator as a function of the input power. Such a strategy is numerically very convenient, since the first step gives a single valued relation between N and $|C_t|^2$; the bistable effects appear only in the final step.

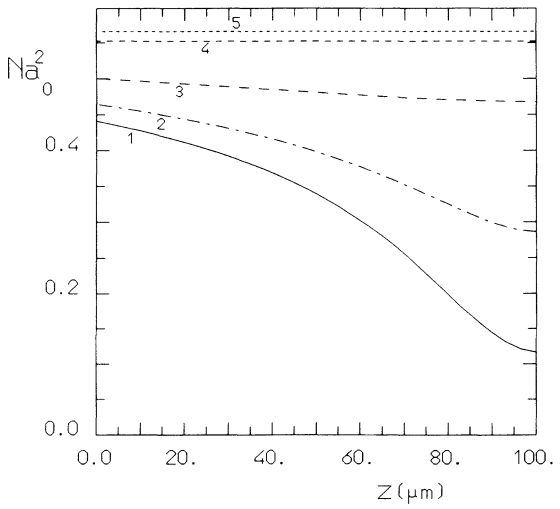

FIG. 6. FP device. Longitudinal carrier distribution $N(z)a_0^2$ for several values of output power $P_t=|C_t|^2$ in mW/μm: (1) $P_t=10^{-3}$, (2) $P_t=10^{-2}$, (3) $P_t=10^{-1}$, (4) $P_t=1$, (5) $P_t=10$. Parameter values: $L=100\,\mu$m, $|S_{11}|^2=0.9$, $\Delta=-0.7$.

C. DFB case

In a distributed-feedback device a grating introduces coupling between the forward and the backward slowly varying amplitudes C_F and C_B [hence $|K|\neq 0$ in Eqs. (4)]; in the stationary case the longitudinal profiles of the amplitudes are described by setting $\partial/\partial t=0$ in Eqs. (4):

$$\frac{\partial C_F}{\partial z}=+[h(z)-\alpha_i]C_F+KC_Be^{i\delta z/L}, \tag{17a}$$

$$\frac{\partial C_B}{\partial z}=-[h(z)-\alpha_i]C_B+K^*C_Fe^{-i\delta z/L}, \tag{17b}$$

where

$$\delta=-\Delta\beta L=(p\beta_g-2\beta_0)L \tag{18}$$

is the normalized detuning between the grating and the mode propagation constants; in this way the definition of δ corresponds precisely to that of the FP case [Eq. (15)] provided that ω_c/v_g is replaced by $p\beta_g/2$. In addition, because of the absence of mirrors, the internal amplitudes are related to the incident, reflected, and transmitted amplitudes by the boundary conditions

$$\begin{aligned}&C_F(0)=C_i,\quad C_F(L)=C_t,\\&C_B(0)=C_r,\quad C_B(L)=0,\end{aligned} \tag{19}$$

where $z=0$ and L are the longitudinal coordinates at the beginning and at the end of the grating. In this case no simple analytical solution can be found. Therefore we compute $|C_i|^2$ and $|C_r|^2$ as a function of $|C_t|^2$ by integration of the differential equations (17) from $z=L$ to 0 using a standard computer algorithm, because the boundary condition in $z=L$ depends only on C_t. Finally, as in

the FP case, the transmission and reflection properties of the DFB device as a function of the input power $|C_i|^2$ are obtained by inverting the function $|C_i|^2=\mathcal{F}(|C_t|^2)$.

The carrier density $N(z)$ necessary to compute $h(z)$ is determined by solving numerically, with a false position method [31], the equation

$$R(N)-\frac{\eta}{\hbar v_g}\,\mathrm{Im}\left[\frac{\Delta\epsilon(N)}{\epsilon}\right][|C_F(z)|^2+|C_B(z)|^2]=0\ , \tag{20}$$

obtained from (7) by dropping the derivative.

An example of the forward ($|C_F(z)|^2$) and backward ($|C_B(z)|^2$) longitudinal power distributions are shown in Figs. 7(a) and 7(b) for two values of the output power, which correspond to dots *a* and *b* on curve 3 in Fig. 12,

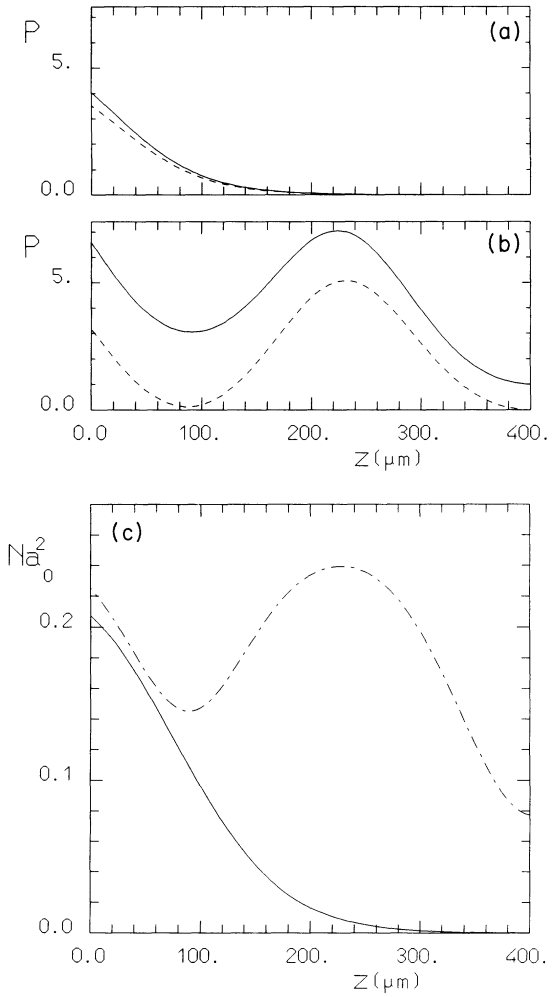

FIG. 7. DFB device. (a) and (b) longitudinal distributions for forward (solid line) and backward (dashed line) power (in mW/μm) for two values of the output power P_t, corresponding to dots (a) and (b) of curve (3) in Fig. 12. (c) longitudinal distribution of density of carriers $N(z)a_0^2$ for two values of the output power P_t, corresponding to dots (a) (solid line) and (b) (dashed line) of the same curve in Fig. 12. Parameter values: $L=400$ μm, $K=150\ \mathrm{cm}^{-1}$, $\Delta=-3$, $\delta=56$.

while the longitudinal distributions of the normalized carrier density for the same output powers are shown in Fig. 7(c). Contrary to the FP case, the backward field shows a z dependence similar to that of the forward field. At low power levels there is a strong absorption and therefore only a limited portion of the device is useful. At high power levels, because of the saturation and of the strong coupling between forward and backward fields, the whole length is useful and the fields and carrier density show multiple undulations which become more pronounced as the power is increased.

IV. NUMERICAL RESULTS

A. FP case

Optical transmission and reflection static responses for the FP resonator represented in Figs. 1(a) and 1(b) and having a transverse index profile like the one reported in Fig. 15 have been numerically computed by varying the most important parameters which influence the device behavior.

First of all the effect of varying the working frequency, represented in our model by the parameter Δ, has been investigated. Typical results regarding the transmitted power $P_t=|C_t|^2$ as a function of the incident power $P_i=|C_i|^2$ (in mW/μm) are shown in Figs. 8(a)–8(c); logarithmic scales have been used in order to show in a unique diagram several curves, for a wide range of parameters, so to allow an easy comparison. The Δ values chosen are -0.7 (excitonic absorption peak) in Fig. 8(a), -2 in Fig. 8(b), and -3 in Fig. 8(c). The curves in each diagram refer to different values of detuning δ [see Eq. (15)]; the range of δ has been chosen in each case so to present bistability effects. A rough idea of the δ values needed to get hysteretic behavior can be obtained by imposing that, at the power level corresponding to saturation of absorption (and hence also saturation of the refractive index Δn), the transmission given by Eq. (13) is a maximum (resonance condition), i.e.,

$$\delta\simeq 2\int_0^L \mathrm{Im}[h(z)]dz+2\pi p'\ ,$$

where p' is an integer properly chosen as required by the condition $|\delta|<\pi$. This expression can be easily evaluated with the assumption of a constant $h(z)$; as a matter of fact, as it clearly appears from Fig. 6, at high power levels $N(z)$ reduces to a constant, owing to the saturation of the absorption. As a consequence of the large variation of the refractive index, the value of the index p' that must be chosen to have $|\delta|<\pi$ can be of some units. Note that the frequency spacing between adjacent cavity modes $\pi v_g/L$, multiplied by $\hbar$ and divided by E_x (see the definition of Δ in Sec. II), amounts to 0.12 for $L=100$ μm. Therefore, as it appears from Fig. 2(b), the excitonic resonance covers several modes of the cavity.

Bistable behavior occurs in all the reported cases, due to the high nonlinearity of the field-carrier interaction in the QW. However near the excitonic resonance [Fig. 8(a)], the presence of a strong absorption produces a rather narrow hysteresis cycle with respect to the input

power, even if the output contrast can be high. For the other values of Δ [Figs. 8(b) and 8(c)] the cycles are more symmetrical and bistability can be achieved at lower input power levels (even less than 1 mW/μm; typical value of input contrast can be 3, while at the output it is always larger. Very similar cycles can be observed for $\Delta=-2$ and -3; the first case, because of the larger refractive index change, displays wider cycles, but, owing to the still large absorption, a greater input power is required to achieve the same level of output power. By working even further from the exciton peak, the bistable behavior degrades as a consequence of the reduced nonlinearity (smaller change of Δn, as shown in Fig. 4). For the preceding reasons, the following numerical results will be presented for $\Delta=-3$.

Figures 9(a) and 9(b) show, respectively, the transmission and reflection characteristics obtained by varying the mirror reflectivity. As is well known, the hysteretic behavior appears only for reflectivities larger than a threshold value, in our case slightly less than 0.8. By increasing $|S_{11}|^2$, the hysteresis cycle becomes more and more pronounced, but an increasing input level is required to commute the output. Similar considerations apply to the dependence of reflected power $P_r=|C_r|^2$ on the input power P_i [Fig. 9(b)], showing clearly a complementary character with respect to P_t (i.e., high P_r when P_t is low,

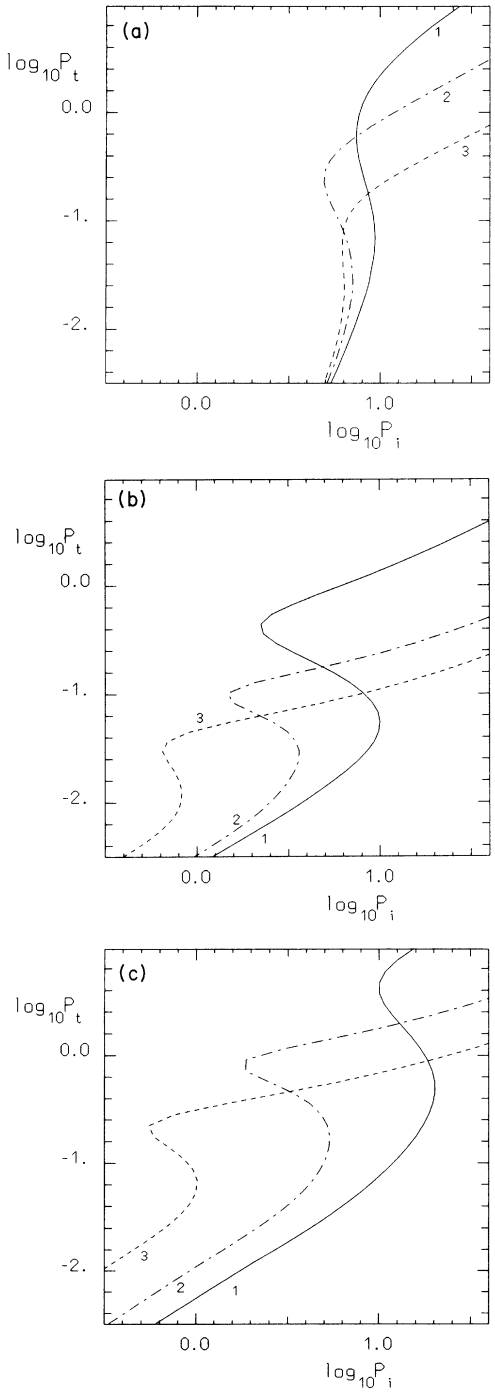

FIG. 8. FP device. Transmitted power P_t as a function of input power P_i, in mW/μm (with logarithmic scales) for $L=50$ μm, $|S_{11}|^2=0.9$, and different values for the parameters Δ (i.e., working frequency) and δ (see text). (a) $\Delta=-0.7$: (1) $\delta=-1.42$, (2) $\delta=-0.94$, (3) $\delta=-0.47$; (b) $\Delta=-2$: (1) $\delta=-1.18$, (2) $\delta=-0.24$, (3) $\delta=0.71$; (c) $\Delta=-3$: (1) $\delta=-1.65$, (2) $\delta=-1.18$, (3) $\delta=-0.71$.

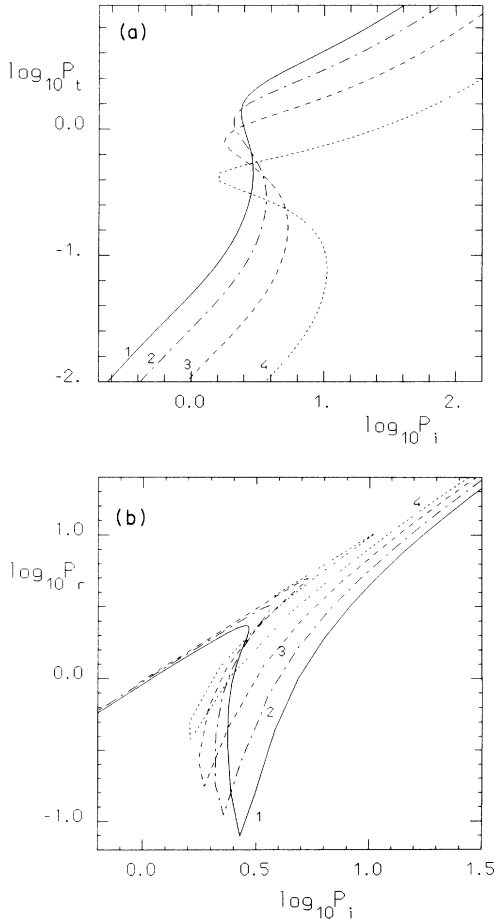

FIG. 9. FP device. (a) transmitted power P_t and (b) reflected power P_r as a function of input power P_i, in mW/μm (with logarithmic scales) for $L=50$ μm, $\Delta=-3$, $\delta=1.56$ and for several values of the mirror reflectivity $|S_{11}|^2$: (1) $|S_{11}|^2=0.80$, (2) $|S_{11}|^2=0.85$, (3) $|S_{11}|^2=0.90$, (4) $|S_{11}|^2=0.95$.

and vice versa).

The effect of varying the resonator length is shown in Figs. 10(a) and 10(b). Also in this case there is a required minimum value of the parameter to achieve bistability (in our case, approximately $L=30\ \mu$m). By increasing L, the cycle becomes more and more pronounced and, with rather high values of resonator length, a second hysteresis cycle appears. This is due to the large refractive index nonlinearity in the QW structure that, associated with a large L, allows to exploit more than one longitudinal resonance; by further increasing L the system can show multiple hysteresis cycles.

B. DFB case

We have also analyzed the static responses in transmission and reflection for the DFB device represented in Fig. 1(c), with the same material parameters of the FP device.

In Fig. 11 typical curves of transmitted power P_t as a function of input power P_i are shown for three different values of working frequency, corresponding to $\Delta=-3$, -2, and -1. Each curve, in logarithmic scale for the same reason as for the FP case, is calculated with a different value of the parameter δ of Eq. (18) which measures the detuning between the grating and the input frequency. Precisely, for each Δ the value of δ is chosen with the criterion of obtaining the largest size for the bistability hysteresis cycle (i.e., the largest S-shaped curve).

We can calculate approximately these optimum values for δ in the following way. By neglecting the absorption $(\mathrm{Re}(h)-\alpha_i)$ and assuming the function $h(z)$ constant over the full length of the device, Eqs. (17), with the boundary conditions (19), can be easily integrated, and we obtain expressions for the transmission ($\mathcal{T}$) and reflection ($\mathcal{R}$) coefficients of the device:

$$\mathcal{R}=\left|\frac{C_r}{C_i}\right|^2=1-\mathcal{T}\ ,$$
$$\mathcal{T}=\left|\frac{C_t}{C_i}\right|^2=\left|\frac{\sqrt{1-\gamma^2}}{\sqrt{1-\gamma^2}\cosh(|K|L\sqrt{1-\gamma^2})-i\gamma\sinh(|K|L\sqrt{1-\gamma^2})}\right|^2\ , \tag{21}$$

where

$$\gamma=\frac{1}{|K|}\left[\mathrm{Im}(h)-\frac{\delta}{2L}\right]\ .$$

It is simple to see that $\mathcal{T}\simeq 0$ if $|\gamma|\le 1$ and $\mathcal{T}=1$ for

$$|\gamma|=\left[1+\left[\frac{l\pi}{|K|L}\right]^2\right]^{1/2}\qquad l=1,2,\ldots\ . \tag{22}$$

Because $\mathrm{Im}(h)$ diminishes when the density of carriers increases, as one can see from Fig. 2(b), in order to ensure the maximum output contrast, there must be low transmitted power when the carrier density is at its minimum, and on the contrary high transmitted power when the carrier density is saturated; so the subsequent condition [obtained choosing $l=1$ in Eq. (22)] must be fulfilled:

$$\frac{1}{|K|}\left[\frac{\delta}{2L}-\mathrm{Im}(h_s)\right]\simeq\left[1+\left[\frac{\pi}{|K|L}\right]^2\right]^{1/2}\ ,$$

where h_s is the value of $h(N)$ on saturation of the carrier density. From this expression we obtain

$$\delta_{\mathrm{opt}}\simeq 2(|K|^2L^2+\pi^2)^{1/2}+2L\ \mathrm{Im}(h_s)\ . \tag{23}$$

This formula gives a straightforward way to obtain the best operating values for δ as a function of the device parameters K and L, and it is used for the calculation of the following results.

As one can see from Fig. 11 bistable behavior is possible in a DFB device only if the input frequency is far from excitonic resonance; in fact for $\Delta=-3$ the hysteresis cycle is bigger, and has a very large output contrast, but it disappears completely when $\Delta=-1$; the size of the cycle is comparable with those of FP devices, but it needs a higher input power, often more than 1 mW/μm, because to achieve bistability a DFB device must be generally longer and the absorptive effects are more important, as will be shown in the following. In order to analyze the influence of the other parameters of the device, we choose in the following the value $\Delta=-3$ (as for the FP case) in which we have the largest S-shaped curves.

In Fig. 12 we show the transmission characteristics of this system by varying the detuning δ; the range of values in which one has bistable behavior is approximately 10 around the optimum value $\delta_{\mathrm{opt}}=52$ (with $|K|=150\ \mathrm{cm}^{-1}$ and $L=400\ \mu$m). In fact, as one can guess from the preceding discussion, the effect of the refractive nonlinearity is important only in this range δ, and in particular for $\delta<\delta_{\mathrm{opt}}$ the transmission of the device is at its minimum because one has $|\gamma|<1$ on saturation of the carrier density, and consequently $\mathcal{T}\simeq 0$ from Eq. (21).

The effect of varying the coupling coefficient $|K|$ is shown in Fig. 13(a) for the transmitted power; the bistable behavior appears only if $|K|$ is larger than a threshold value (in this case $\simeq 60\ \mathrm{cm}^{-1}$), becomes more pronounced and requires more input power as $|K|$ increases, and finally the cycle becomes narrower and disappears when $|K|$ becomes definitely larger than 200 cm^{-1}. The same behavior is evident also in the dependence of the reflected power P_r on the input power, as shown in Fig. 13(b). In Figs. 14(a) and 14(b) we show, respectively the transmission and reflection characteristic obtained by varying the device length; the hysteresis cy-

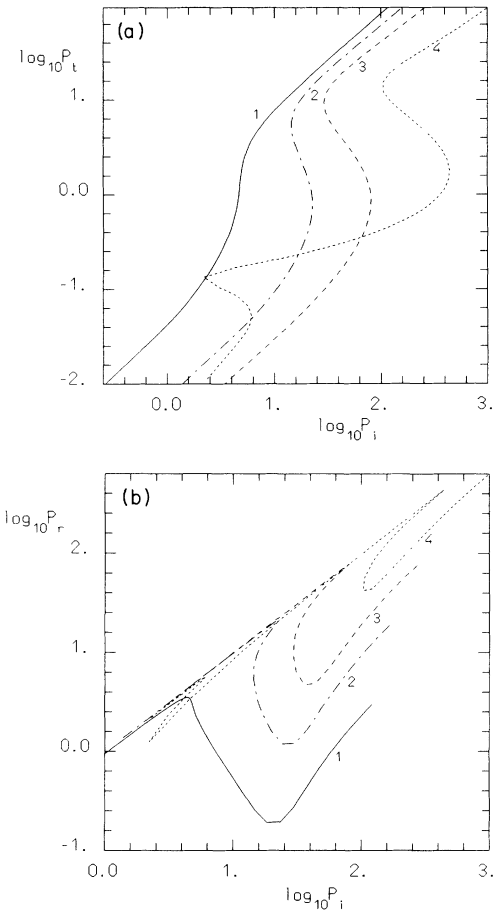

FIG. 10. FP device. (a) transmitted power P_t and (b) reflected power P_r as a function of input power P_i, in mW/μm (with logarithmic scales) for $|S_{11}|^2=0.9$, $\Delta=-3$, and for different values of device length L (in μm) with δ properly chosen. (1) $L=20$, $\delta=1.88$; (2) $L=50$, $\delta=-1.56$; (3) $L=100$, $\delta=-3.11$; (4) $L=300$, $\delta=-3.05$.

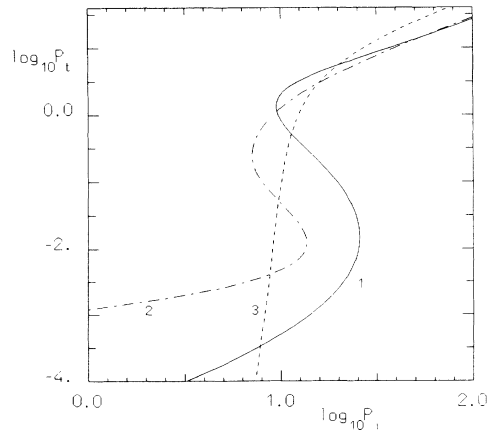

FIG. 11. DFB device. Transmitted power P_t as a function of input power P_i, in mW/μm (with logarithmic scales) for $L=400$ μm, $|K|=150$ cm^{-1}, and different values for the parameter Δ (i.e., working frequency), with δ properly chosen (see text); (1) $\Delta=-3$, $\delta=52$; (2) $\Delta=-2$, $\delta=53$; (3) $\Delta=-1$, $\delta=56$.

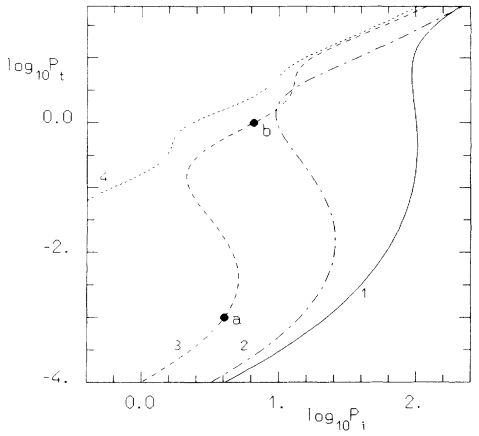

FIG. 12. DFB device. Transmitted power P_t as a function of input power P_i, in mW/μm (with logarithmic scales) for $\Delta=-3$, $L=400$ μm, $|K|=150$ cm^{-1}, and several values of the detuning δ: (1) $\delta=50$, (2) $\delta=52$, (3) $\delta=56$, (4) $\delta=62$. The dots (a) and (b) on curve (3) refer to Figs. 7(a)–7(c).

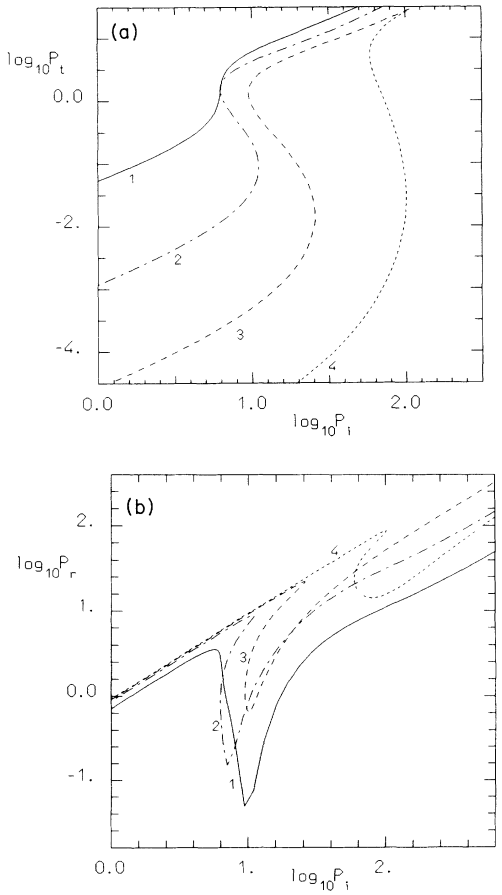

FIG. 13. DFB device. (a) transmitted power P_t and (b) reflected power P_r as a function of input power P_i, in mW/μm (with logarithmic scales) for $\Delta=-3$, $L=400$ μm, and different values of the coupling constant $|K|$ in cm^{-1}, with δ properly chosen (see text). (1) $|K|=50$, $\delta=48$; (2) $|K|=100$, $\delta=50$; (3) $|K|=150$, $\delta=52$; (4) $|K|=200$, $\delta=54$.

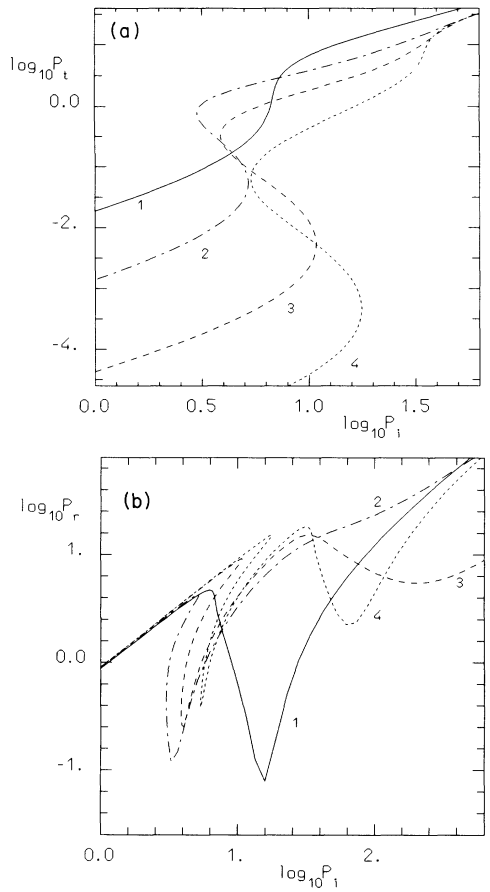

FIG. 14. DFB device. (a) transmitted power P_t and (b) reflected power P_r as a function of input power P_i, in mW/μm (with logarithmic scales) for $\Delta=-3$, $|K|=150$ cm^{-1}, and different values of the device length L in μm, with δ properly chosen (see text). (1) $L=200$, $\delta=28$; (2) $L=300$, $\delta=42$; (3) $L=400$, $\delta=54$; (4) $L=500$, $\delta=66$.

cle becomes larger with the increase of the coupling length, over the threshold value $L=200$ μm. As one can see from Fig. 14(b), for large values of L a second hysteresis cycle initiates to appear, due to the presence of the other peaks of the transmission coefficient $\mathcal{T}=1$, corresponding to the choice $l=2,3,\ldots$ in Eq. (22). However, by further increasing L, only the primary cycle survives, and in a more restricted range of δ, because of the increased absorption.

V. CONCLUSIONS

The bistable behavior discussed in this paper arises from the interaction of the optical field with the excitonic resonance, which gives rise simultaneously to dispersion and absorption. Very illuminating for the understanding of the behavior of the system are the diagrams in Figs. 3 and 4, which show the behavior of the absorption coefficient α and of the refractive index Δn as a function of the local power. The examination of these curves leads to the conclusion that the bistability observed here is basically of the dispersive type. As a matter of fact, even when the input field is near resonance with the excitonic line the refractive index Δn exhibits a noteworthy variation as a function of the optical power (curves 3 and 4 in Fig. 4). However, because the absorption is large in these cases (curves 3 and 4 in Fig. 3) the hysteresis cycles turn out to be rather narrow and the bistability is not very pronounced. Much better cycles are obtained when the input field is substantially detuned from the excitonic peak, so that absorption is strongly reduced (curves 1 and 2 in Fig. 3). On the other hand, when the detuning from the excitonic peak becomes too large also the variation of the refractive index as a function of power is reduced. Therefore one finds an optimal range of values for the detuning Δ between the input field and the excitonic resonance; the cases shown in Figs. 8(b) and 8(c) lie in this range.

In this paper we considered both the case of a Fabry-Pérot resonator and the case of a distributed-feedback device. It is not straightforward to make a general comparison between the two devices. Let us compare, for example, curve 2 in Fig 8(c) and curve 1 in Fig. 11; both of them are obtained for $\Delta=-3$. We see that the size of the cycle is similar in the two cases; the DFB device requires a larger input power to obtain switching to the high transmission state, but exhibits a large output contrast. In practice, it may be easier to obtain a bistable device in the DFB configuration, because it is not simple to realize the required high reflectivity at the endfacets of the sample in the FP case.

In this article we did not discuss at all the stability of the stationary solutions. We mentioned in Sec. IV A that, in the conditions considered here, several cavity modes lie below the excitonic resonance. It is well known [2] that in this situation the system may develop instabilities induced by the growth of cavity modes different from that which contributes to the stationary state. The stability analysis of the stationary solutions is planned to be performed in the future.

ACKNOWLEDGMENTS

We are grateful to Izo Abram, Domenico Campi, Elsa Garmire, Hartmut Haug, Peter Koch, and Jean-Louis Oudar for illuminating discussions and suggestions. This research was carried out in the framework of the "Progetto Finalizzato Telecomunicazioni" of the Consiglio Nazionale delle Ricerche.

APPENDIX

Following the general approach of Ref. [30], but including also a slow time variation in the amplitudes, the transverse electric and magnetic fields in the waveguide under analysis are expanded in the complete set of transverse modes E_n and H_n (n denotes the mode order and t means transverse to z):

$$E_t = e^{-i\omega t}\left[\sum_n C_{Fn}(z,t)e^{i\beta_n z} + \sum_n C_{Bn}(z,t)e^{-i\beta_n z}\right]E_n + \text{c.c.}\,,$$
$$H_t = e^{-i\omega t}\left[\sum_n C_{Fn}(z,t)e^{i\beta_n z} - \sum_n C_{Bn}(z,t)e^{-i\beta_n z}\right]H_n + \text{c.c.} \qquad (24)$$

with β_n being the propagation constants; β_n, E_n, and H_n all refer to the mean angular frequency ω and correspond to a "reference waveguide" which, in our case, is a planar waveguide having the cross section of Fig. 1(a) and the refractive index profile represented in Fig. 15, in the case of six wells. The effect of the nonlinear interaction and of a possible grating are introduced in the model as sources of dielectric polarization. In our case they are related, respectively, to $\Delta\epsilon$ given in Eq. (1) for the nonlinearity in one well and to $\Delta\epsilon_g^{(p)}$ in Eq. (6) for the grating effect [see Fig. 1 (c)]; these quantities are the permittivity changes with respect to the "reference waveguide." By introducing such sources and the preceding field expansions in the Maxwell equations and by using the orthonormality relations for the field distributions, a complete set of coupled equations for the coefficients C_{Fn} and C_{Bn} are obtained; the procedure is completely similar to the one developed, for instance, in [30], but in our case including the slow time variation of the field amplitudes. When only one transverse mode plays a significant role, as assumed in the present paper, and the unperturbed dielectric medium is isotropic and lossless, the equations and coupling coefficients are those given in Eqs. (4)–(6) of the text.

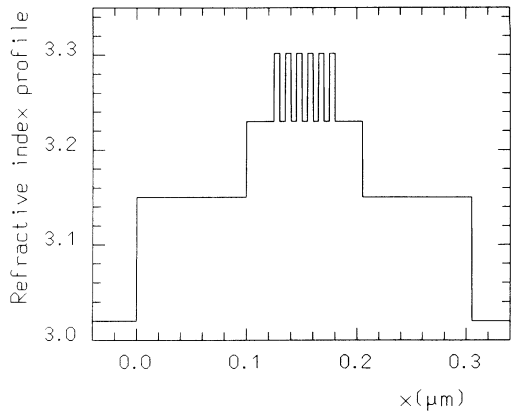

FIG. 15. Unperturbed refractive index profile for six wells.

*Permanent address: Dipartimento di Fisica, Università degli Studi di Milano, via Celoria 16, 20133 Milano, Italy.

[1] E. Abraham and S. D. Smith, Rep. Prog. Phys. **45**, 815 (1982).
[2] L. A. Lugiato, in *Progress in Optics,* edited by E. Wolf (North-Holland, Amsterdam, 1984) Vol. XXI, p. 69ff.
[3] H. M. Gibbs, *Optical Bistability: Controlling Light With Light* (Academic, New York, 1985).
[4] R. Bonifacio and L. A. Lugiato, Opt. Commun. **19**, 172 (1976); R. Bonifacio and L. A. Lugiato, Lett. Nuovo Cimento **21**, 517 (1978).
[5] D. S. Chemla, D. A. B. Miller, P. W. Smith, A. C. Gossard, and W. Wiegmann, IEEE J. Quantum Electron. **QE-20**, 265 (1984); D. S. Chemla and D. A. B. Miller, J. Opt. Soc. Am. B **2**, 1155 (1985).
[6] D. S. Chemla, D. A. B. Miller, and P. W. Smith, Opt. Eng. **24**, 556 (1985).
[7] J. P. Pocholle, M. Razeghi, J. Raffy, M. Papuchon, C. Weisbuch, C. Puech, A. Vandenborre, J. L. Bezy, L. Heinrich, and J. E. Vimont, Rev. Phys. Appl. **22**, 1239 (1987).
[8] S. Schmitt-Rink, D. S. Chemla, and D. A. B. Miller, Phys. Rev. B **32**, 6601 (1985).
[9] J. Goll and H. Haken, Phys. Status Solidi B **101**, 489 (1980).
[10] E. Garmire, IEEE J. Quantum Electron. **QE-25**, 289 (1989).
[11] H. Yokoyama, IEEE J. Quantum Electron. **QE-25**, 1190 (1989).
[12] P. K. Milsom and A. Miller, Opt. Quantum Electron. **21**, 81 (1989).
[13] J. L. Oudar, B. Sfez, R. Kuszelewicz, J. C. Michel, and R. Azoulay, Phys. Status Solidi B **159**, 181 (1990).
[14] A. Empsten and I. Veretennicoff, IEEE J. Quantum Electron. **QE-26**, 1089 (1990).
[15] H. G. Winful, J. H. Marburger, and E. Garmire, Appl. Phys. Lett. **35**, 379 (1979).
[16] G. I. Stegemann, C. Liao, and H. G. Winful, in *Optical Bistability II,* edited by C. M. Bowden, H. M. Gibbs, and S. L. McCall (Plenum, New York, 1984), p. 329.
[17] A. Mecozzi, S. Trillo, and S. Wabnitz, Opt. Lett. **12**, 1008 (1987).
[18] A. Empsten and I. Veretennicoff, Proc. SPIE, **1127**, 29 (1990).
[19] G. P. Bava and L. A. Lugiato, Opt. Commun. **78**, 195 (1990).
[20] H. Haug and S. Schmitt-Rink, J. Opt. Soc. Am. B **2**, 1135 (1985).
[21] S. Schmitt-Rink and C. Ell, J. Lumin. **30**, 585 (1985).
[22] S. Schmitt-Rink, C. Ell, and H. Haug, Phys. Rev. B **33**, 1183 (1986).
[23] H. Haug and S. W. Koch, Phys. Rev. A **39**, 1887 (1989).
[24] C. Ell, R. Blank, S. Benner, and H. Haug, J. Opt. Soc. Am. B **6**, 2006 (1989).
[25] H. Haug and S. W. Koch, *Quantum Theory of the Optical and Electronic Properties of Semiconductors* (World Scientific, Singapore, 1990).
[26] G. P. Bava and P. Debernardi, Electron. Lett. **27**, 603 (1991).
[27] M. Asada, A. Kayemada, and Y. Suematsu, IEEE J. Quantum Electron. **QE-20**, 745 (1984).
[28] M. Asada, IEEE J. Quantum Electron. **QE-25**, 2019 (1989).
[29] G. D. Sanders and Y. Chang, Phys. Rev. B **32**, 5517 (1985).
[30] D. Marcuse, *Theory of Dielectric Optical Waveguide* (Academic, New York, 1974).
[31] W. H. Press, B. P. Flannery, S. A. Teukolsky, and W. T. Vetterling, *Numerical Recipes* (Cambridge University Press, Cambridge, 1986).